Mechanism and Machine Theory 94 (2015) 96–118

Contents lists available at ScienceDirect

Mechanism and Machine Theory

journal homepage: www.elsevier.com/locate/mechmt

Seamless dual brake transmission for electric vehicles: Design, control and experiment

Mir Saman Rahimi Mousavi *, Ali Pakniyat, Tao Wang, Benoit Boulet

Department of Electrical and Computer Engineering, McGill University, 817 Sherbrooke St. West, Montréal, QC H3A 0C3, Canada
Centre for Intelligent Machines, McGill University, 817 Sherbrooke St. West, Montréal, QC H3A 0C3, Canada

A R T I C L E I N F O

Article history:
Received 13 January 2015
Received in revised form 25 May 2015
Accepted 7 August 2015
Available online 29 August 2015

Keywords:
Two-speed seamless transmission
Electric vehicle
Dynamical modeling
Pontryagin Minimum Principle
Backstepping controller

A B S T R A C T

Transmission is one of the crucial elements of a motor vehicle's driveline that affects efficiency and dynamic performance of the vehicle. This paper studies the dynamical modeling, controller design, and experimental validation of a two-speed transmission for electric vehicles which has a specification of seamless gear shifting. The transmission incorporates a two-stage planetary gear set with common sun and common ring gears and two braking mechanisms to control the flow of power. The dynamical modeling of the driveline of an electric vehicle equipped with such a transmission is derived by exploiting the torque balance and virtual work principle. Thereafter, the Pontryagin Minimum Principle is applied to design an optimal shifting controller. This controller keeps the output speed and the output torque of the driveline constant during the gear shifting operation while minimizing the shifting time and the dissipation of energy caused by the internal brakes. Since the optimal control law provided by the Minimum Principle is open loop, a backstepping controller is designed to provide a stabilizing feedback law based on the optimal control inputs. Simulation and experimental results demonstrate the ability of the proposed transmission to exhibit smooth shifting without excessive oscillations in the output speed and torque.

1. Introduction

Increasing fuel cost and environmental concerns have pushed the automotive industry to gradually replace internal combustion engine (ICE) vehicles with hybrid electric (HEV) and fully electric vehicles (EV). However, the energy density of electric batteries is much less than that of fossil fuels. Thus, by changing the source of power from internal combustion engine to electric motor, it is required to minimize the losses in the driveline in order to maximize the range of EVs. Pure electric vehicles in the market are mostly equipped with single ratio transmission with a trade-off between efficiency and dynamic performance, such as maximum speed, acceleration, and gradability [1]. Research indicates that using multi-speed transmission for EVs can reduce the size of the electric motor and provide an appropriate balance between the efficiency and the dynamic performance [1–5]. Currently used multi-speed transmissions for EVs such as Automated Manual Transmission (AMT), Automatic Transmission (AT), Dual Clutch Transmission (DCT), and Continuously Variable Transmission (CVT) were initially designed for ICE vehicles [6]. Since ICEs cannot operate below certain speeds and their speed control during gear changes is not an easy task, the presence of clutches or torque convertors is inevitable for start-ups, idle running and gear changing. This, however, is not the case for EVs as electric motors are speed controllable in a wide range of operating speeds. This difference provides an opportunity for designing novel transmissions for EVs [4,5].

* Corresponding author at: McConnell Engineering Bldg., room 503, Department of Electrical and Computer Engineering, McGill University, 817 Sherbrooke St. West, Montréal, QC H3A 0C3, Canada.
E-mail addresses: mir.rahimimousavi@mail.mcgill.ca, saman@cim.mcgill.ca (M.S. Rahimi Mousavi), pakniyat@cim.mcgill.ca (A. Pakniyat), tao.wang6@mcgill.ca (T. Wang), benoit.boulet@mcgill.ca (B. Boulet).

http://dx.doi.org/10.1016/j.mechmachtheory.2015.08.003

AMT is of great interest because of its lower weight and higher efficiency in comparison with other types of transmissions such as AT, CVT and DCT [7–9]. However, the torque interruption during gear changing operation, which comes from the disengagement and re-engagement of the transmission to the electric motor or engine, reduces passenger comfort and lifetime of the synchronizers. Gear shifting and drivability improvement of a clutchless AMT for EVs are addressed in [10] via a sliding mode controller that reduces the gap of torque interruption (shifting time). The same problem is tackled in [11] by using a combination of state-feedback and H_∞ robust controllers to provide an optimal speed synchronization. A comparison between a fixed-ratio transmission and a novel two-speed I-AMT (Inverse Automated Manual Transmission) with rear mounted dry clutches is made in [3] and dynamic programming is used to design the optimal gear ratios for the first and second gears in order to minimize the energy consumption for urban and sub-urban drive cycles. It is indicated that efficiency and dynamic performance of a two-speed AMT transmission with optimal gear ratios are much better than those of a single speed transmission.

In contrast to AMT, DCT has the special feature of eliminating the output torque interruption during gear shifts, but they have lower efficiency and higher weight [12–14]. A two-speed DCT transmission for electric vehicles is studied in [15] and an open-loop shifting controller is presented. The results demonstrate that the vibration of the output torque is not considerable and the torque hole is almost eliminated.

Continuously variable transmissions (CVTs) provide continuous change of the gear ratio. The principle used by CVT transmission is to keep the source of power (electric motor or engine) in the most efficient point while changing the gear ratio in order to get different combinations of the torque and speed. However, since the set of efficient operating points for electric motors is rich enough multiplicity of gear ratios or a continuously variable transmission are not necessary for EVs [16–19].

Similar to DCTs, planetary-gear-based ATs have the ability to eliminate the output torque interruption during the gear shift operation. However, due to the existence of torque convertors and hydraulic systems in ATs, they generally have lower efficiency in comparison with other types of transmissions and they are not of great interest for EVs. Although the presence of torque convertor provides passenger comfort and increases drivability, the output power of the transmission can be decreased due to internal slippage inside the torque convertor when it is not completely locked-up [6,20–23].

This paper proposes a compact two-speed clutchless seamless transmission in order to meet a desirable efficiency, performance, and drivability for EVs. This transmission is comprised of a dual-stage planetary gear set with common ring and common sun gears. The ratio of the pitch diameter of the ring gear to the sun gear in the input and output sides are different in order to provide two different gear ratios. A special feature of planetary gear trains is the possession of high power density due to the torque distribution over several gears which provides a compact design [6]. Two friction brakes are considered to direct the flow of power during gearshift through the control of the speed of the sun and the ring gears such that a fast and smooth gear change is achieved. The proposed design is such that the transmission is perpetually connected to the electric motor and final drive and there is no clutch or torque converter to disconnect this mechanical coupling.

The gear shift control through torque and inertia phases is the conventional control strategy employed for ATs and DCTs [24]. The control of the proposed transmission through these phases is studied in [4]. Because of the perpetual connectedness of the power transmission paths in this transmission, torques and speeds are always dependent on each other through the transmitted power. Hence, the control strategy can be further improved such that the control strategy would not be required to be distinctly separated into the torque and inertia phases. This forms the basis for the controller design in this paper.

Fig. 1 shows the schematic view of the driveline of an electric vehicle equipped with the proposed two-speed transmission. As can be seen in Fig. 1, the input of the transmission is the carrier of the first stage of the two-stage planetary gear set, which is attached to an electric motor. The output of the mechanism is the carrier of the second stage which is connected via the final drive to the wheels. Two different gear ratios can be obtained by braking the sun or the ring gears. As explained in more detail in Section 4 the control of the brakes can be made in such a way that the gear shifting would be seamless and without any torque interruption. Fig. 2 shows a 3D exploded view diagram of the proposed transmission. Here, for brevity, the terms sun, ring and planets are used instead of sun gear, ring gear and planet gears, respectively.

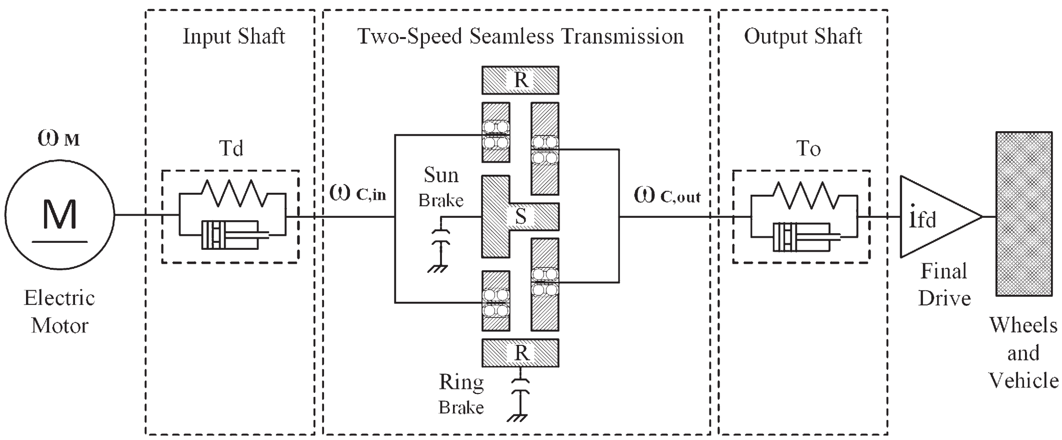

Fig. 1. The driveline of an EV equipped with the proposed two-speed transmission.

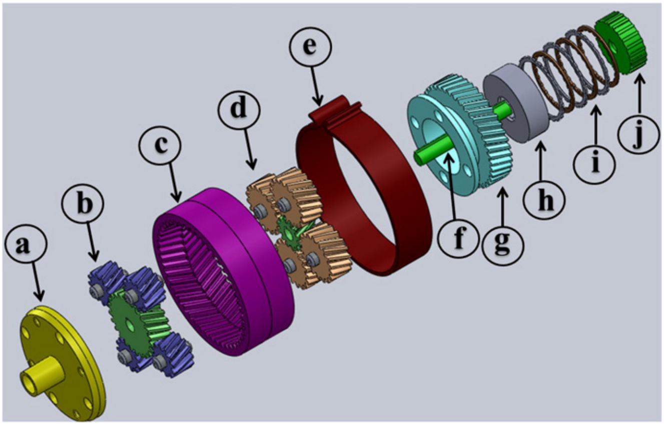

Fig. 2. 3D exploded view diagram: a) input carrier, b) first stage planetary gear set, c) common ring gear, d) second stage planetary gear set, e) band brake, f) common shaft for sun gears, g) output carrier, h) outer hub for the sun brake, i) friction plates and j) inner hub for the sun brake.

The kinematic analysis of the two-stage planetary gear set is studied in Section 2. In this section, the achievable gear ratios of the transmission are presented as a function of the ratios of the first and second planetary gear sets. In Section 3, a dynamical model of the driveline of an electric vehicle equipped with such a transmission is developed for subsequent use in the controller design in Section 4. In this section, optimal control problems are formulated and the Pontryagin Minimum Principle (PMP) is employed to design the optimal control for minimizing the shifting time and the energy dissipation caused by the internal brakes during the gear change while keeping the output torque and the output speed of the driveline constant. Based on the results of the optimal controller, the backstepping method is applied to design a closed-loop asymptotically stable controller which copes with the actuator limitations. Simulation and experimental results are provided in Section 5 to validate the performance of the controller and the seamless behavior of the proposed transmission.

2. Kinematic analysis and gear ratios

2.1. Kinematic equations

In this section, the kinematic equations of the dual-stage planetary gear set and the achievable gear ratios are studied in order to be utilized in the dynamical modeling of the proposed transmission. The kinematic relations between the components of a single stage planetary gear set, such as Carrier (C), Sun (S), Planets (P), and Ring (R) are [25]:

$$r_R\omega_R = r_P\omega_P + r_C\omega_C; \quad r_R = r_P + r_C \tag{1}$$

$$r_C\omega_C = r_P\omega_P + r_S\omega_S; \quad r_C = r_P + r_S \tag{2}$$

where r_S, r_P, and r_R are the pitch radii of the sun, planet, and ring, respectively. The parameter r_C is the radius of the circle on which the planets are mounted. The variables ω_S, ω_P, ω_R, and ω_C are the angular velocities of the sun, planets, ring, and carrier, respectively. By eliminating ω_P and r_P from Eqs. (1) and (2), the kinematic relation between the ring, the sun, and the carrier is as follows:

$$(r_R + r_S)\omega_C = r_S\omega_S + r_R\omega_R \tag{3}$$

For simplification of the formulation, the ratio of the pitch radius of the ring (r_R) to the sun (r_S) for the first and the second stages of the planetary gear sets are defined as:

$$R_1 := \left(\frac{r_R}{r_S}\right)_{1\text{st}\,stage}; R_2 := \left(\frac{r_R}{r_S}\right)_{2\text{nd}\,stage}. \tag{4}$$

It is obvious that R_1 and R_2 are greater than 1 since the pitch radius of the ring is always greater than the sun's.

During the gear changing process, the transmission has two degrees of freedom, hence it is required to select two generalized coordinates to derive the equations of motion. In this paper, the generalized coordinates are chosen to be $q = [\theta_S\,\theta_R]^T$, where θ_S and θ_R are the angular displacements of the sun and the ring, respectively and accordingly, all the angular velocities are expressed as functions of ω_S and ω_R. From Eqs. (1)–(4) the angular velocities of the input carrier ($\omega_{C,in}$), the output carrier ($\omega_{C,out}$), the input planets ($\omega_{P,in}$), and the output planets ($\omega_{P,out}$) can be expressed as angular velocities of the sun (ω_S) and the ring (ω_R) as follows:

$$\begin{cases} \omega_{C,in} = \dfrac{R_1\omega_R + \omega_S}{(R_1+1)}; & \omega_{C,out} = \dfrac{R_2\omega_R + \omega_S}{(R_2+1)} \\ \omega_{P,in} = \dfrac{R_1\omega_R - \omega_S}{(R_1-1)}; & \omega_{P,out} = \dfrac{R_2\omega_R - \omega_S}{(R_2-1)} \end{cases}. \tag{5}$$

2.2. Gear ratios

According to equation set (5), the gear ratio of the transmission (the ratio of the input speed to the output speed) can be expressed as follows:

$$\frac{\omega_{C,in}}{\omega_{C,out}} = \frac{(R_2+1)(\omega_S + R_1\omega_R)}{(R_1+1)(\omega_S + R_2\omega_R)}. \tag{6}$$

According to Eq. (6), three different gear ratios are achievable:

1 If the ring is completely grounded ($\omega_R = 0$):

$$\frac{\omega_{C,in}}{\omega_{C,out}} = \frac{(R_2+1)}{(R_1+1)} = GR_1. \tag{7}$$

2 If the sun is completely grounded $\omega_S = 0$:

$$\frac{\omega_{C,in}}{\omega_{C,out}} = \frac{(R_2+1)R_1}{(R_1+1)R_2} = GR_2. \tag{8}$$

3 If neither the sun nor the ring is grounded ($\omega_R \neq 0$ and $\omega_S \neq 0$):

$$\frac{\omega_{C,in}}{\omega_{C,out}} = \frac{(R_2+1)(\omega_S + R_1\omega_R)}{(R_1+1)(\omega_S + R_2\omega_R)} = GR_T. \tag{9}$$

Here, GR_1 and GR_2 are considered as the first and the second gear ratios where GR_T is the transient gear ratio from the first gear ratio to the second one during the gear shifting process. Although the gear ratios are dependent, it is possible to solve Eqs. (7) and (8) for R_1 and R_2 in order to get the desired GR_1 and GR_2. Fig. 3 shows the achievable GR_1 and GR_2 by varying R_1 and R_2 from 1 to 10, and the selected gear ratios in this paper.

The effect of gear ratio selection on the efficiency and dynamic performance is studied in [1] where genetic algorithms are used in order to determine the optimal range of gear ratios for a pure electric vehicle with a 75 kW permanent magnet AC motor and equipped with a two-speed transmission. The results show that the dynamic performance is highly dependent on the gear ratio selection while

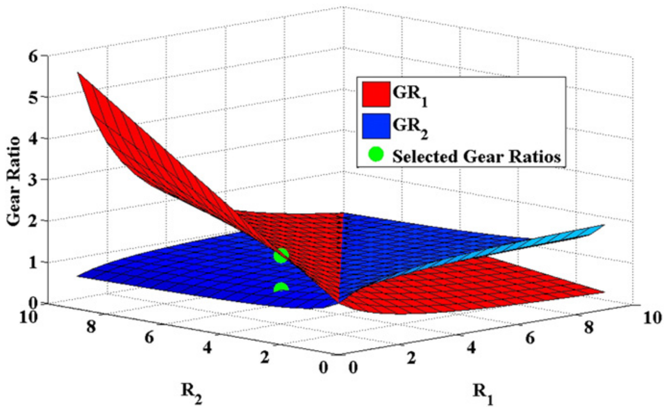

Fig. 3. Achievable GR_1 and GR_2 by varying R_1 and R_2.

efficiency is not considerably affected by the transmission gear ratios. The possibility of improving the dynamic performance of EVs is an advantage of multi-speed transmissions compared to single speed ones [26].

As it can be observed in Fig. 3, except for the line $R_1 = R_2$, one of the gear ratios expressed in Eqs. (7) and (8) is always overdrive and the other one is underdrive.

In this paper $R_1 = 2$ and $R_2 = 4$ are selected to provide $GR_1 = 1.667$ and $GR_2 = 0.833$ to be used in both simulation and experimental analyses. These gear ratios are multiplied by the final drive ratio i_{fd} to give the overall gear ratios of the driveline in the vehicle. Hence, the desired overall gear ratios can be obtained by appropriate selection of R_1, R_2, and i_{fd}.

For instance, with the selection $R_1 = 2$, $R_2 = 4$, and $i_{fd} = 5$ the resulting overall gear ratios are $GR_1 = 8.333$ and $GR_2 = 4.167$ which lie within the optimal ranges for the two-speed electric vehicle reported in [1].

3. Dynamical modeling of the driveline

As it can be seen in Fig. 1, the driveline is comprised of an electric motor, a flexible input shaft, the two-speed seamless transmission, a flexible output shaft, a final drive, and wheels. In this section, the dynamic model of the driveline is presented in order to be employed for the controller design purposes.

3.1. Electric motor and flexible input shaft

The electric motor is the only source of power in this driveline. The dynamics of the motor can be expressed by using the torque balance equation as follows:

$$\dot{\omega}_M = \frac{T_M - T_d}{J_M} \tag{10}$$

where J_M and T_M are the inertia and the electromagnetic torque of the motor, respectively. Here, T_d is the drive torque which can be considered as the load on the motor and can be calculated as follows:

$$T_d = K_d\left(\theta_M - \theta_{C,in}\right) + B_d\left(\omega_M - \omega_{C,in}\right) \tag{11}$$

where K_d and B_d are the equivalent torsional stiffness and damping constants of the flexible input shaft and θ_M and $\theta_{C,in}$ are the angular displacements of the motor and the input carrier. By differentiating Eq. (11) with respect to time and assuming the damping term to be negligible [27], the torque rate of the drive torque can be considered as follows:

$$\dot{T}_d \approx K_d\left(\omega_M - \omega_{C,in}\right). \tag{12}$$

3.2. Two-speed seamless transmission

By considering the generalized coordinates to be $q = [\theta_S\ \theta_R]^T$, where θ_S and θ_R are the angular displacements of the sun and the ring gears, and by neglecting the stiffness of the gears, the principle of virtual work can be applied to derive the dynamic equation of the two-speed transmission. The principle of virtual work states that for a system with m number of generalized coordinates q_k, $k \in \{1, \ldots, m\}$ [28]:

$$\sum_{k=1}^{m}\left[Q_k^{appl,nc} - \frac{d}{dt}\left(\frac{\partial L}{\partial \dot{q}_k}\right) + \frac{\partial L}{\partial q_k}\right]\delta q_k = 0 \tag{13}$$

where $L = T - V$ is the Lagrangian, T and V are the total kinetic and potential energy of the system. $Q_k^{appl,nc}$ and δq_k are the non-conservative applied torques and virtual displacements, respectively.

By considering the center of mass of the system as the reference point for the gravitational energy and by considering all the mechanical parts inside the transmission to be rigid, the total potential energy of the system remains constant ($V = 0$). The kinetic energy of the system consists of the kinetic energy of the input and output carriers, the ring, the sun, the four input and four output planets as follows:

$$T = \frac{1}{2}I_{C,in}\omega_{C,in}^2 + \frac{1}{2}I_{C,out}\omega_{C,out}^2 + \frac{1}{2}I_R\omega_R^2 + 4\left(\frac{1}{2}I_{P,in}\omega_{P,in}^2 + \frac{1}{2}m_{P,in}r_{C,in}^2\omega_{C,in}^2\right) + \frac{1}{2}I_S\omega_S^2 + 4\left(\frac{1}{2}I_{P,out}\omega_{P,out}^2 + \frac{1}{2}m_{P,out}r_{C,out}^2\omega_{C,out}^2\right). \tag{14}$$

In Eq. (14), $I_{C,in}$, $I_{C,out}$, I_S, I_R, $I_{P,in}$, and $I_{P,out}$ are the moment of inertia of the input carrier, output carrier, sun, ring, input planets, and output planets, respectively; $m_{P,in}$ and $m_{P,out}$ are the mass of the input and output planets. In terms of the generalized coordinates introduced earlier, the kinetic energy is written as:

$$\begin{aligned}T=&\frac{1}{2}\left(I_{C,in}+4m_{P,in}r_{C,in}^{2}\right)\left(\frac{\omega_S^2+R_1^2\omega_R^2+2R_1\omega_R\omega_S}{(R_1+1)^2}\right)\\&+\frac{1}{2}\left(I_{C,out}+4m_{P,out}r_{C,out}^{2}\right)\left(\frac{\omega_S^2+R_2^2\omega_R^2+2R_2\omega_R\omega_S}{(R_2+1)^2}\right)\\&+4\left\{\frac{1}{2}I_{P,in}\left(\frac{\omega_S^2+R_1^2\omega_R^2-2R_1\omega_R\omega_S}{(R_2-1)^2}\right)+\frac{1}{2}I_S\omega_S^2\right.\\&+4\left\{\frac{1}{2}I_{P,out}\left(\frac{\omega_S^2+R_2^2\omega_R^2-2R_2\omega_R\omega_S}{(R_2-1)^2}\right)+\frac{1}{2}I_R\omega_R^2.\right.\end{aligned}\tag{15}$$

By using the principle of virtual work in Eq. (13), the equations of motion for the two generalized coordinates $q=[\theta_S\ \theta_R]^T$ can be written as follows:

$$\begin{cases}\dot{\omega}_S=\dfrac{1}{a}\left(T_{BS}\tau-T_{BR}\lambda-\omega_S C_S\tau+\omega_R C_R\lambda+cT_d-dT_o+T_{Sf}\tau-T_{Rf}\lambda\right)\\ \dot{\omega}_R=\dfrac{1}{a}(T_{BR}\gamma-T_{BS}\lambda+\omega_S C_S\lambda-\omega_R C_R\gamma+eT_d-fT_o+T_{Rf}\gamma-T_{Sf}\lambda\end{cases}\tag{16}$$

in which the coefficients are listed in Table 1. In Eq. (16), C_S, C_R, T_{Sf}, and T_{Rf} are the coefficients of the viscous and Coulomb friction of the transmission measured from experimental tests and T_o is the output torque of the transmission.

It should be noted that T_{BS} and T_{BR} are the braking torques of the sun and ring gears.

In the transmission system proposed in this paper, the brake of the sun is designed to be of the multi-plate brake type. Thus, the relation between the normal applied force on the plates and the resulting torque is [29]:

$$T_{BS}=-\mu_P N_{BS}\,n\left(\frac{2}{3}\right)\left(\frac{R_o^3-R_i^3}{R_o^2-R_i^2}\right)sign(\omega_S);\quad N_{BS}\geq 0\tag{17}$$

where μ_P is the coefficient of friction between the plates, N_{BS} is the applied normal brake force to the plates and n is the number of the friction surfaces. The inner and outer radii of the multi-plate brake are denoted by R_i and R_o, respectively. The brake of the ring is designed to be of band brake type, resulting in the relation between the applied normal force at the end of the band and the resulting torque in the form of [29]:

$$\begin{cases}T_{BR}=-N_{BR}R_D\left(e^{\mu_D\theta_D}-1\right);\omega_R\geq 0,\quad N_{BR}\geq 0\\ T_{BR}=N_{BR}R_D\left(1-e^{-\mu_D\theta_D}\right);\omega_R<0,\quad N_{BR}\geq 0\end{cases}\tag{18}$$

where N_{BR} is the force applied at the end of the band, R_D is the radius of the drum brake, μ_D is the coefficient of friction between band and drum and θ_D is the angle of wrap.

For the band brake, the positive direction of rotation is considered as the energizing mode of the band brake.

In order to avoid the undesirable drag torque in both brakes, particularly in the multi-plate brake, they are designed to be of the dry type [30–32].

Fig. 4 shows how engaging and disengaging the brakes of sun (T_{BS}) and ring (T_{BR}) change the path of power transmission and consequently the gear ratio.

Table 1
The coefficient of the dynamical modeling of the two-speed transmission.

$\alpha=\frac{(I_{C,in}+4m_{P,in}r_{C,in}^2)}{(R_1+1)^2}$	$\psi=\frac{4I_{P,out}}{(R_2-1)^2}$
$\beta=\frac{(I_{C,out}+4m_{P,out}r_{C,out}^2)}{(R_2+1)^2}$	$a=(\gamma\tau-\lambda^2)$
$\gamma=[I_S+\alpha+\beta+\phi+\psi]$	$c=\frac{\tau-R_1\lambda}{R_1+1}$
$\tau=[I_R+(\alpha+\phi)R_1^2+(\beta+\psi)R_2^2]$	$d=\frac{\tau-R_2\lambda}{R_2+1}$
$\lambda=[(\alpha-\phi)R_1+(\beta-\psi)R_2]$	$e=\frac{\gamma R_1-\lambda}{R_1+1}$
$\phi=\frac{4I_{P,in}}{(R_1-1)^2}$	$f=\frac{\gamma R_2-\lambda}{R_2+1}$

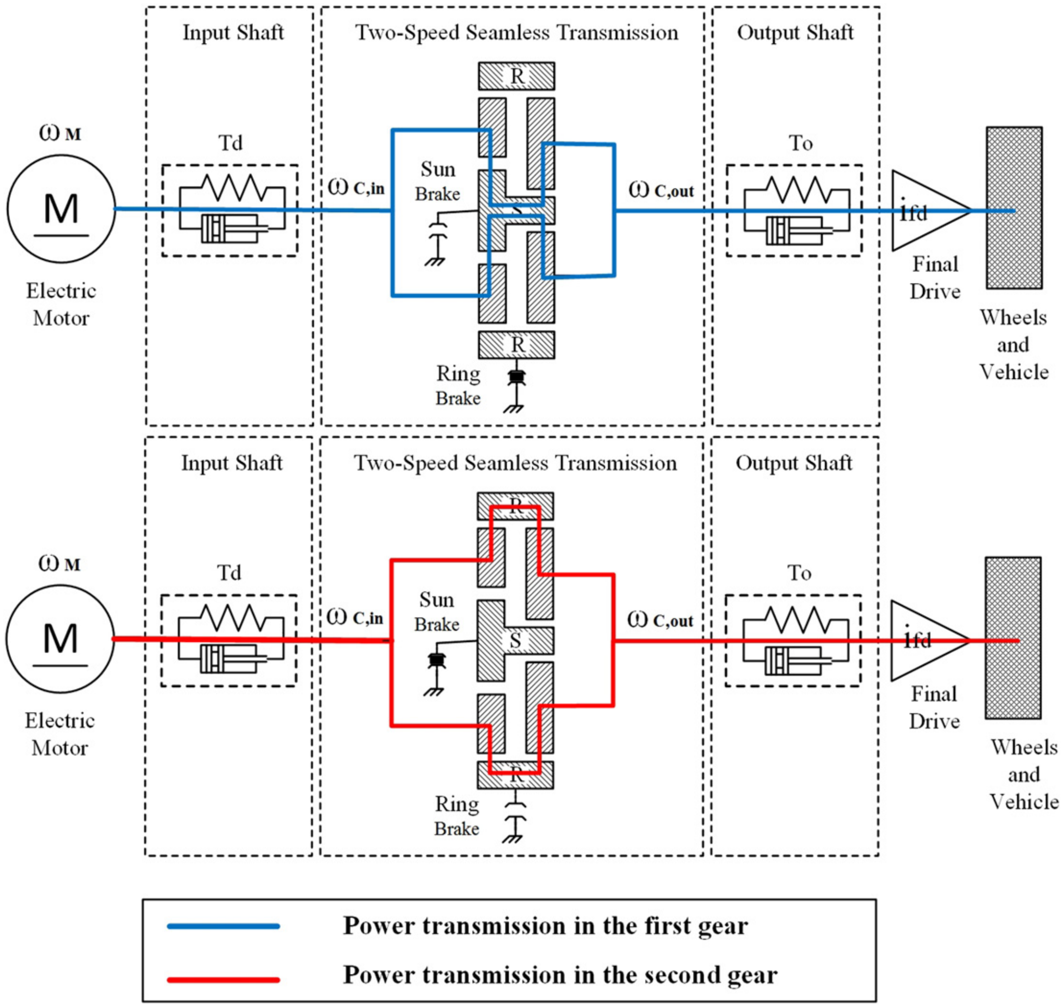

Fig. 4. Power transmission path.

3.3. Vehicle dynamics and flexible output shaft

By using lumped mass method [27] and the torque balance equation, the dynamics of the vehicle can be expressed as follows:

$$\dot{\omega}_w = \frac{T_o i_{fd} - T_v}{J_v} \tag{19}$$

where J_v is the inertia of the vehicle and wheels, i_{fd} is the final drive ratio and T_v is the resisting torque on the vehicle that can be calculated from the following relation [33,34]:

$$T_v = R_w \left(\frac{1}{2} \rho v_x^2 C_d A_f + m_v g \sin(\theta_{road}) + K_r m_v g \cos(\theta_{road}) \right). \tag{20}$$

In Eq. (20), R_w, θ_{road}, K_r, m_v, v_x, ρ, C_d and A_f indicate wheel radius, road angle, tire rolling resistance, vehicle mass, vehicle velocity, air density, aerodynamic drag coefficient and vehicle frontal area. Slip of the tires are neglected so the geometric relation $v_x = R_w \omega_w$ can be considered between the angular velocity of the wheels and the speed of the vehicle for the straight motion. The output torque of the transmission, denoted T_o, can be calculated from the following equation:

$$T_o = K_o \left(\theta_{C,out} - i_{fd} \theta_w \right) + B_o \left(\omega_{C,out} - i_{fd} \omega_w \right) \tag{21}$$

where K_o and B_o are the equivalent torsional stiffness and damping constants of the flexible output shaft and $\theta_{C,out}$ and θ_w are the angular displacements of the output carrier and the wheels. By differentiating Eq. (21) with respect to time and assuming the damping term to be negligible [27], the torque rate of the output torque of the transmission can be considered as follows:

$$\dot{T}_o \approx K_o\left(\omega_{C,out} - i_{fd}\omega_w\right). \tag{22}$$

By collecting Eqs. (10), (12), (16), (19) and (22) together, the full state dynamics of the system are as follows:

$$\begin{cases} \dot{\omega}_M = \dfrac{-1}{J_M}T_d + \dfrac{1}{J_M}T_M \\ \dot{T}_d = K_d\omega_M - \dfrac{K_d}{R_1+1}\omega_S - \dfrac{K_dR_1}{R_1+1}\omega_R \\ \dot{\omega}_S = \dfrac{-C_S\tau}{a}\omega_S + \dfrac{C_R\lambda}{a}\omega_R + \dfrac{c}{a}T_d - \dfrac{d}{a}T_o \\ \qquad + \dfrac{\tau}{a}\left(T_{BS} + T_{Sf}\right) - \dfrac{\lambda}{a}\left(T_{BR} + T_{Rf}\right) \\ \dot{\omega}_R = \dfrac{C_S\lambda}{a}\omega_S - \dfrac{C_R\gamma}{a}\omega_R + \dfrac{e}{a}T_d - \dfrac{f}{a}T_o \\ \qquad - \dfrac{\lambda}{a}\left(T_{BS} + T_{Sf}\right) + \dfrac{\gamma}{a}\left(T_{BR} + T_{Rf}\right) \\ \dot{T}_o = -i_{fd}K_o\omega_w + \dfrac{K_o}{R_2+1}\omega_S + \dfrac{K_oR_2}{R_2+1}\omega_R \\ \dot{\omega}_w = -\dfrac{1}{J_v}T_v + \dfrac{i_{fd}}{J_v}T_o. \end{cases} \tag{23}$$

4. Controller design

As explained earlier, the proposed transmission has the ability to change the gear while transmitting the power from the motor to the wheels without any torque or speed interruption in the output. This goal, together with the minimization of the shifting time and the energy dissipation caused by internal brakes of the transmission during gear changing is formulated in the optimal control framework in Sections 4.1 and 4.2 which forms the basis for the general control strategy in Section 4.3.

4.1. Preliminaries for the optimal controller design

For simplicity of notation, the problem is formulated for the case when the resisting torque from the road (T_v) on the vehicle is constant during the gear shifting and accordingly the output torque and output speed of the driveline are desired to remain constant during the gear changing. These requirements are interpreted as $\dot{\omega}_w = 0$ and $\dot{T}_o = 0$ and hence from Eqs. (5) and (23) these control requirements are expressed as:

$$T_o = \frac{1}{i_{fd}}T_v \tag{24}$$

and

$$\omega_{C,out} = i_{fd}\omega_w. \tag{25}$$

The constant value for $\omega_{C,out}$ in Eq. (25) necessarily requires that (see Eq. (5)):

$$\omega_R = \left(\frac{R_2+1}{R_2}\right)i_{fd}\omega_w - \frac{1}{R_2}\omega_S \tag{26}$$

as well as:

$$\dot{\omega}_{C,out} = 0 \Rightarrow \dot{\omega}_R = \frac{-1}{R_2}\dot{\omega}_S. \tag{27}$$

The objective of the control is to go from an initial gear into a target gear (i.e., from Eqs. (7) to (8) through Eq. (9) and vice versa) by means of engaging and releasing the brakes. For the states ω_S and ω_R in Eq. (23) the initial and terminal conditions can be expressed as:

$$\begin{bmatrix} \omega_S \\ \omega_R \end{bmatrix} = \begin{bmatrix} \omega_{S_{(@\ GR_1)}} \\ 0 \end{bmatrix} \underset{downshift}{\overset{upshift}{\rightleftharpoons}} \begin{bmatrix} \omega_S \\ \omega_R \end{bmatrix} = \begin{bmatrix} 0 \\ \omega_{R_{(@\ GR_2)}} \end{bmatrix}. \tag{28}$$

From Eqs. (27) and (23) the following equation can be derived:

$$(\lambda R_2 - \tau)(C_S\omega_S - T_{BS}) - (\gamma R_2 - \lambda)(C_R\omega_R - T_{BR}) + (c + eR_2)T_d - (\lambda R_2 - \tau)T_{Sf} + (\gamma R_2 - \lambda)T_{Rf} - (d + fR_2)T_o = 0. \tag{29}$$

Rearranging Eq. (29) gives:

$$T_d = \frac{1}{c + eR_2}\Big((\lambda R_2 - \tau)T_{BS} + (\lambda - \gamma R_2)T_{BR} + (\tau - \lambda R_2)C_S\omega_S + (\gamma R_2 - \lambda)C_R\omega_R + (\lambda R_2 - \tau)T_{Sf} - (\gamma R_2 - \lambda)T_{Rf} + (d + fR_2)T_o\Big). \tag{30}$$

The controllability of Eq. (23) implies that there exist a motor torque T_M such that Eq. (30) is satisfied for all instants (see [5] and also Section 4.3 of this paper and Eq. (83)). Thus, among the control inputs, the motor torque T_M is reserved for satisfying Eq. (30), and hence the number of independent control inputs is reduced to two, i.e., the brakes of the sun and ring T_{BS} and T_{BR}.

Substituting T_d from Eq. (30) and ω_R from Eq. (5) into the equation for $\dot{\omega}_S$ in Eq. (23) results in:

$$\begin{aligned} \dot{\omega}_S = \frac{1}{a(c + eR_2)}\big(&-[(e\tau + c\lambda)C_SR_2 + (e\lambda + c\gamma)C_R]\omega_S - (de - cf)R_2T_o \\ &+ (1 + R_2)(e\lambda + c\gamma)C_R\omega_{C,out} + (e\tau + c\lambda)R_2T_{BS} - (e\lambda + c\gamma)R_2T_{BR} \\ &+ (e\tau + c\lambda)R_2T_{Sf} - (e\lambda + c\gamma)R_2T_{Rf}\big). \end{aligned} \tag{31}$$

For the ease of notation, the coefficients in Eq. (31) are denoted by

$$\begin{cases} A_S := \dfrac{(e\tau + c\lambda)C_SR_2 + (e\lambda + c\gamma)C_R}{a(c + eR_2)} \\ B_{S1} := \dfrac{(e\tau + c\lambda)R_2}{a(c + eR_2)}, \quad B_{S2} := \dfrac{(e\lambda + c\gamma)R_2}{a(c + eR_2)} \\ G_S := \dfrac{1}{a(c + eR_2)}\Big((1 + R_2)(e\lambda + c\gamma)C_R\omega_{C,out} \\ -(de - cf)R_2T_o + (e\tau + c\lambda)R_2T_{Sf} - (e\lambda + c\gamma)R_2T_{Rf}\Big) \end{cases}.$$

Thus Eq. (31) is represented by

$$\dot{\omega}_S = -A_S\omega_S + B_{S1}T_{BS} - B_{S2}T_{BR} + G_S \tag{32}$$

with the initial and the terminal conditions from Eq. (28):

$$\omega_S(t_0) = \omega_{S_{(@GR_1)}}; \quad \omega_S\left(t_f\right) = 0 \tag{33}$$

for the upshift and:

$$\omega_S(t_0) = 0; \quad \omega_S\left(t_f\right) = \omega_{S_{(@GR_2)}} \tag{34}$$

for the downshift processes. The times t_0 and t_f indicate the initial and terminal instances of the gear changing process.

It is assumed that during the gear changing process the ring and the sun are rotating in the positive directions and hence according to Eq. (17) and (18) it can be concluded that:

$$-\left|T_{BS}^{max}\right| \le T_{BS} \le 0, \quad -\left|T_{BR}^{max}\right| \le T_{BR} \le 0. \tag{35}$$

4.2. Optimal control problem

The Pontryagin Minimum Principle states that for a system with the dynamics equation:

$$\dot{x}\,(t) = f(x(t), u(t), t) \tag{36}$$

and the cost functional

$$J(u) = \int_{t_0}^{t_f} l(x(t), u(t), t)dt + h\left(x\left(t_f\right), t_f\right), \tag{37}$$

there exists an adjoint process p^* for the optimal control input u^* and along the corresponding optimal trajectory x^*, such that:

$$\begin{cases} \dot{x}^*(t) = \dfrac{\partial \mathrm{H}}{\partial p}\left(x^*(t), u^*(t), p^*(t), t\right) \\ \dot{p}^*(t) = -\dfrac{\partial \mathrm{H}}{\partial x}\left(x^*(t), u^*(t), p^*(t), t\right) \\ H\left(x^*(t), u^*(t), p^*(t), t\right) \le H\left(x^*(t), u(t), p^*(t), t\right) \end{cases} \tag{38}$$

for all admissible $u(t)$, where the Hamiltonian H is defined by:

$$\mathrm{H}(x(t), u(t), p(t), t) \triangleq l(x(t), u(t), t) + p^T(t) f(x(t), u(t), t), \tag{39}$$

and the terminal boundary condition

$$\left[H\left(x^*\left(t_f\right), u^*\left(t_f\right), p^*\left(t_f\right), t_f\right) + \frac{\partial h}{\partial t}\left(x^*\left(t_f\right), t_f\right)\right]\delta t_f + \left[\frac{\partial h}{\partial x}\left(x^*\left(t_f\right), t_f\right) - p^*\left(t_f\right)\right]^T \delta x_f = 0 \tag{40}$$

is satisfied [35].

4.2.1. The minimum shifting time problem

The cost functional for the minimum time control problem is [35]:

$$J(u) = \int_{t_0}^{t_f} 1dt, \tag{41}$$

with t_f being the first time after t_0 that the terminal condition in Eqs. (33) and (34) occurs. According to Eqs. (32) and (39), the Hamiltonian is formed as:

$$H(\omega_S, p, T_{BS}, T_{BR}) = 1 + p(-A_S\omega_S + B_{S1}T_{BS} - B_{S2}T_{BR} + G_S). \tag{42}$$

Based on the Pontryagin Minimum Principle, the dynamic of the adjoint process p^* is governed by the following equation:

$$\dot{p}^* = -\frac{\partial H(\omega_S, p^*, T_{BS}, T_{BR})}{\partial \omega_S} = p^* A_S \tag{43}$$

and the Hamiltonian minimization condition results in:

$$H\left(\omega_S^*, p^*, T_{BS}^*, T_{BR}^*\right) \le H\left(\omega_S^*, p^*, T_{BS}, T_{BR}^*\right) \tag{44}$$

for all $-|T_{BS}^{max}| \le T_{BS} \le 0$, and

$$H\left(\omega_S^*, p^*, T_{BS}^*, T_{BR}^*\right) \le H\left(\omega_S^*, p^*, T_{BS}^*, T_{BR}\right) \tag{45}$$

for all $-|T_{BR}^{max}| \le T_{BR} \le 0$. Since this is a fixed terminal value problem, from Eq. (40), the terminal value for the adjoint process is free and

$$H\left(\omega_S^*, p^*, T_{BS}^*, T_{BR}^*\right) = 0 \tag{46}$$

at the final time t_f. This also gives Eq. (46) for all $t \in [t_0\ t_f]$ (see e.g., [36]). Hence, according to Eq. (42):

$$p^*\left(-A_S\omega_S^* + B_{S1}T_{BS}^* - B_{S2}T_{BR}^* + G_S\right) = -1 \tag{47}$$

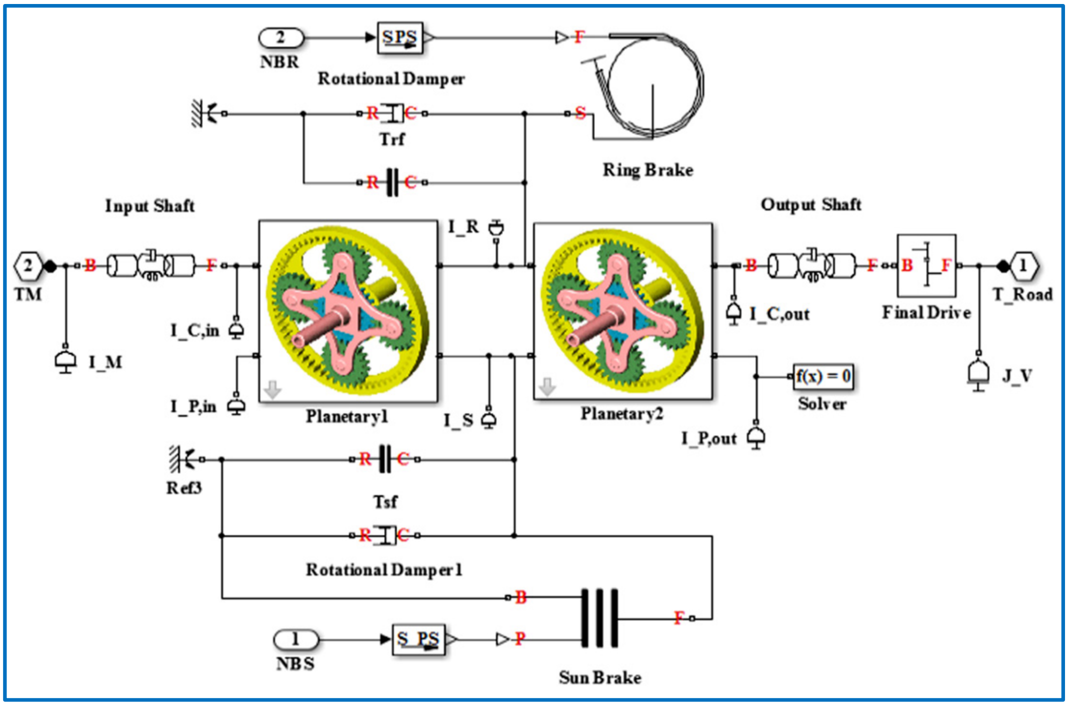

Fig. 5. Driveline model in MATLAB/*Simulink* by utilizing SimDriveLine components.

for all $t \in [t_0\ t_f]$. Solving Eq. (43) results in

$$p^*(t) = p^*\left(t_f\right)e^{A_s\left(t_f - t\right)}. \tag{48}$$

Since the angular velocity of the sun is decreasing in the upshift process ($\dot{\omega}_S \leq 0$), Eq. (47) requires that $p^*(t_0) > 0$ and hence $p^*(t) > 0$ for all $t \in [t_0, t_f]$. Thus the Hamiltonian minimization Eqs. (44) and (45) give $T_{BS}^* = -|T_{BS}^{max}|$ and $T_{BR}^* = 0$, respectively. In a similar way it can be argued that the Hamiltonian minimization Eqs. (44) and (45) give $T_{BS}^* = 0$ and $T_{BR}^* = -|T_{BR}^{max}|$ for the downshift process.

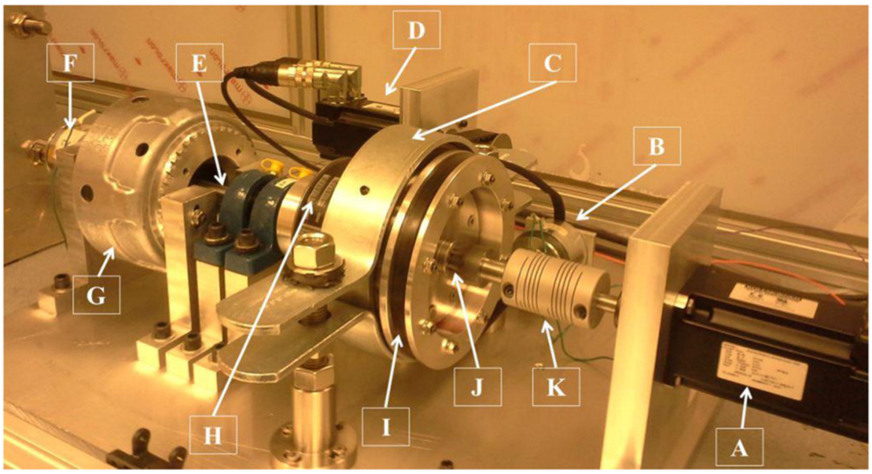

Fig. 6. Experimental testbed. (A) Traction motor, (B) solenoid actuator for the band brake (ring brake), (C) transmission housing, (D) load motor, (E) sun shaft, (F) solenoid actuator for multi-plate brake (sun brake), (G) multi-plate brake pack, (H) output of the transmission (output carrier) and timing belt, (I) band brake, (J) input of the transmission (input carrier) and (K) flexible coupling.

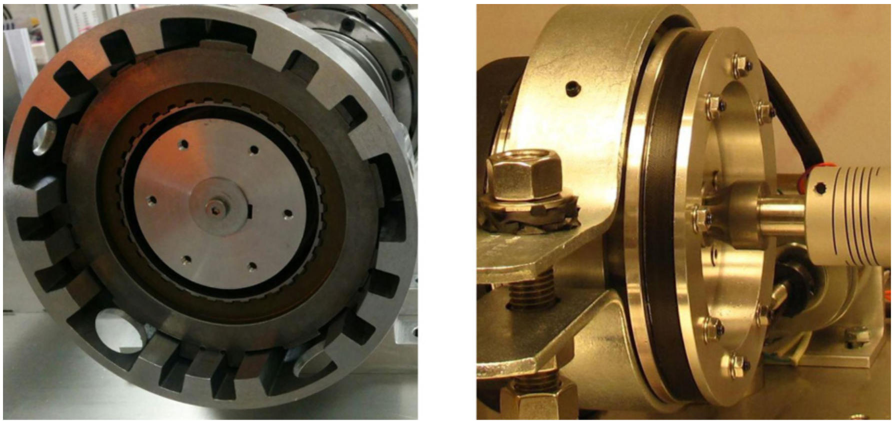

(a) Multi-plate brake for the sun gear (b) Band brake for the ring gear

Fig. 7. Ring and sun gears mounted on the sets of ball bearings.

4.2.2. Minimum energy dissipation controller

For the system (Eq. (32)) with the initial and terminal conditions (Eqs. (33) and (34)), the minimum energy dissipation control problem is equivalent to:

$$\min_u \int_{t_0}^{t_f} -\left(T_{BS}+T_{Sf}\right)\omega_S-\left(T_{BR}+T_{Rf}\right)\omega_R\,dt. \tag{49}$$

Replacing ω_R from Eq. (5) gives the cost functional as

$$\min_u \int_{t_0}^{t_f}\left(-\left(T_{BS}+T_{Sf}-\frac{1}{R_2}\left(T_{BR}+T_{Rf}\right)\right)\omega_S-\left(1+\frac{1}{R_2}\right)\left(T_{BR}+T_{Rf}\right)\omega_{C,out}\right)dt \tag{50}$$

that results in the Hamiltonian in the form:

$$H(\omega_S,p,T_{BS},T_{BR})=p(-A_S\omega_S+B_{S1}T_{BS}-B_{S2}T_{BR}+G_S)-\left(T_{BS}+T_{Sf}-\frac{1}{R_2}\left(T_{BR}+T_{Rf}\right)\right)\omega_S-\left(1+\frac{1}{R_2}\right)\left(T_{BR}+T_{Rf}\right)\omega_{C,out}. \tag{51}$$

Based on the Minimum Principle, the dynamics for the optimal adjoint process p^* is given by:

$$\dot{p}^*=-\frac{\partial H(\omega_S,p^*,T_{BS},T_{BR})}{\partial\omega_S}=p^*A_S+\left(T_{BS}+T_{Sf}-\frac{1}{R_2}\left(T_{BR}+T_{Rf}\right)\right). \tag{52}$$

The Hamiltonian minimization condition with respect to T_{BS} gives

$$(p^*B_{S1}-\omega_S^*)T_{BS}^*\le(p^*B_{S1}-\omega_S^*)T_{BS} \tag{53}$$

for all $-|T_{BS}^{max}|\le T_{BS}\le 0$, and the Hamiltonian minimization with respect to T_{BR} gives

$$\left(-p^*B_{S2}+\frac{\omega_S^*}{R_2}-\left(1+\frac{1}{R_2}\right)\omega_{C,out}\right)T_{BR}^*\le\left(-p^*B_{S2}+\frac{\omega_S^*}{R_2}-\left(1+\frac{1}{R_2}\right)\omega_{C,out}\right)T_{BR} \tag{54}$$

Table 2
Parameters of the experimental apparatus.

$r_{R,in}$ (m)	6e − 2	I_R (kg·m^2)	3e − 3	μ_P	0.14
$r_{R,out}$ (m)	6e − 2	I_S (kg·m^2)	8e − 4	μ_D	0.18
$r_{S,in}$ (m)	3e − 2	$I_{C,in}$ (kg·m^2)	1.4e − 3	n	2
$r_{S,out}$ (m)	15e − 3	$I_{C,out}$ (kg·m^2)	6e − 3	θ_D (rad)	4.014
$r_{P,in}$ (m)	15e − 3	$I_{P,in}$ (kg·m^2)	6.08e − 6	R_i (m)	0.054
$r_{P,out}$ (m)	22.5e − 3	$I_{P,out}$ (kg·m^2)	3.12e − 5	R_o (m)	0.0675
C_R (Nm·s/rad)	0.0034	$m_{P,in}$ (kg)	0.0512	R_D (m)	0.0755
C_S (Nm·s/rad)	0.00105	$m_{P,out}$ (kg)	0.12113	T_{Rf} (Nm)	0.33
K_d (Nm/rad)	161.84	K_o (Nm/rad)	150	T_{Sf} (Nm)	0.12
J_M	5.9e − 5	J_v (kg·m^2)	3.17e − 04	i_{fd}	1

Table 3
Parameters of the backstepping controller.

K_I	K_{II}	K_{III}	K_{IV}	K_V
	1300	1200	2000	3400

for all $-|T_{BR}^{max}| \le T_{BR} \le 0$. With the fixed terminal values specified in Eqs. (33) and (34) the terminal condition Eq. (40) results in:

$$H(\omega_S^*, p^*, T_{BS}^*, T_{BR}^*) = 0 \tag{55}$$

which, similar to the minimum shifting time case, it also holds for all $t \in [t_0\ t_f]$. Noting that $\omega_S^* \ge 0$ for all $t \in [t_0\ t_f]$ and

$$\frac{\omega_S^*}{R_2} - \left(1 + \frac{1}{R_2}\right)\omega_{C,out} \equiv -\omega_R^* \le 0 \tag{56}$$

the optimality conditions (Eqs. (53) and (54)) result in $T_{BS}^* = -|T_{BS}^{max}|$, $T_{BR}^* = 0$ when $p^* \ge \frac{\omega_S^*}{B_{S1}}$ for the upshift operation and $T_{BS}^* = 0$, $T_{BR}^* = -|T_{BR}^{max}|$ when $p^* \le -\frac{\omega_R^*}{B_{S2}}$ for the downshift process. The existence of an adjoint process satisfying Eq. (52) and lying within the region determined by $p^* \ge \frac{\omega_S^*}{B_{S1}}$ for the upshift process and $p^* \le -\frac{\omega_R^*}{B_{S2}}$ for the downshift operation verifies that the minimum energy dissipation controller is equivalent to the minimum shifting time controller.

4.3. Backstepping controller design

Implementation of the optimal control law designed in the previous section is rigorous in practice due to sudden engagement and disengagement of the brakes which eventuate in sudden variation of the motor torque. Therefore in this section, based on the results of the optimal controller, a feasible controller is designed by replacing the sudden engagement and disengagement of the brakes with smooth variations of the braking torques that can be provided by the actuators. The backstepping approach is utilized due to the non-linear and cascade structure of dynamical Eq. (23). The backstepping technique provides a stabilizing feedback law with the simultaneous proof of the stability.

In order to start the recursive procedure of the backstepping controller design, the dynamic equations of ω_w and T_o in Eq. (23) are rewritten according to the kinematic Eq. (5):

$$\begin{cases} \dot{\omega}_w = \dfrac{-1}{J_v}T_v + \dfrac{i_{fd}}{J_v}T_o \\ \dot{T}_o = -i_{fd}K_o\omega_w + K_o\omega_{C,out} \end{cases} . \tag{57}$$

Choosing the first Control Lyapunov Function (CLF) as:

$$V_1(\omega_w) = \frac{1}{2}\left(\omega_w - \omega_{w,des}\right)^2 \tag{58}$$

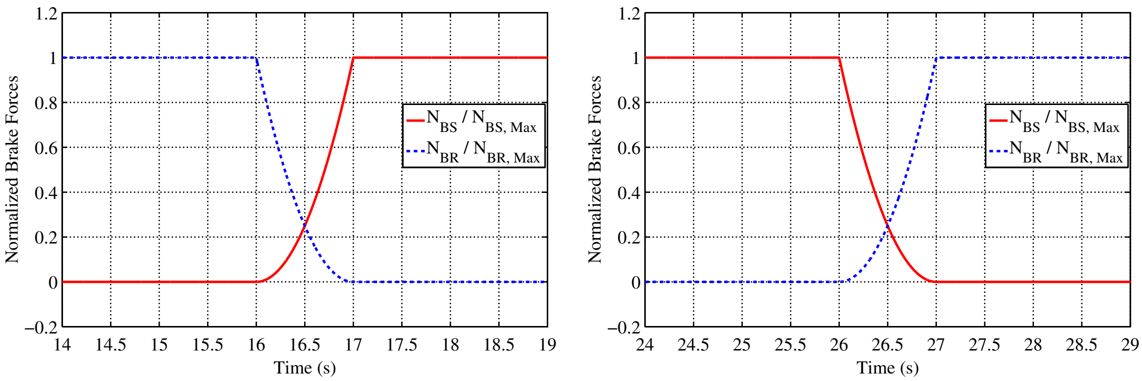

(a) Brake forces during the up shift (b) Brake forces during the down shift

Fig. 8. Normalized brake force profiles applied to both experimental and simulation tests during the upshift and downshift operations.

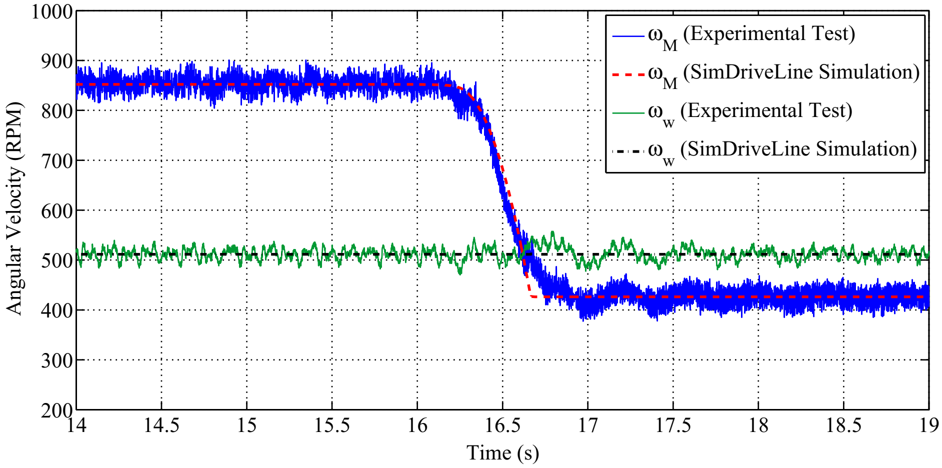

Fig. 9. The motor (ω_M) and output (ω_w) speeds for the upshift operation.

and the virtual control as:

$$\Phi = T_{o,des} = \frac{J_v}{i_{fd}}\left(\frac{1}{J_v}T_v - K_I\left(\omega_w - \omega_{w,des}\right)\right) \tag{59}$$

the time derivative of the Eq. (58) becomes:

$$\dot{V}_1(\omega_w) = -K_I\left(\omega_w - \omega_{w,des}\right)^2 \tag{60}$$

which is clearly negative definite and implies asymptotical stability of ω_w.

Considering the first backstepping change of variables as follows (the backstepping variables are appeared in higher order terms by exploiting the modularity of the method):

$$\varpi = T_o - T_{o,des} = T_o - \Phi. \tag{61}$$

This gives:

$$T_o = \varpi + \Phi \Rightarrow \dot{T}_o = \dot{\varpi} + \dot{\Phi}\,. \tag{62}$$

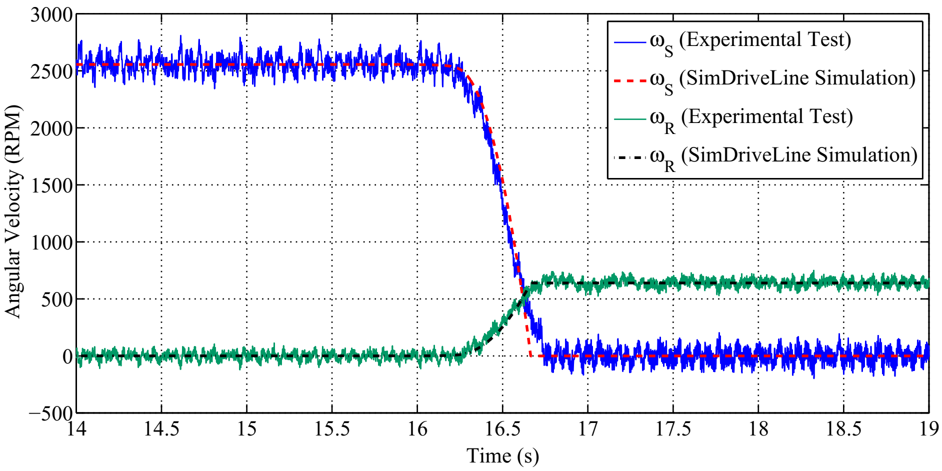

Fig. 10. The ring (ω_R) and sun (ω_S) speeds for the upshift operation.

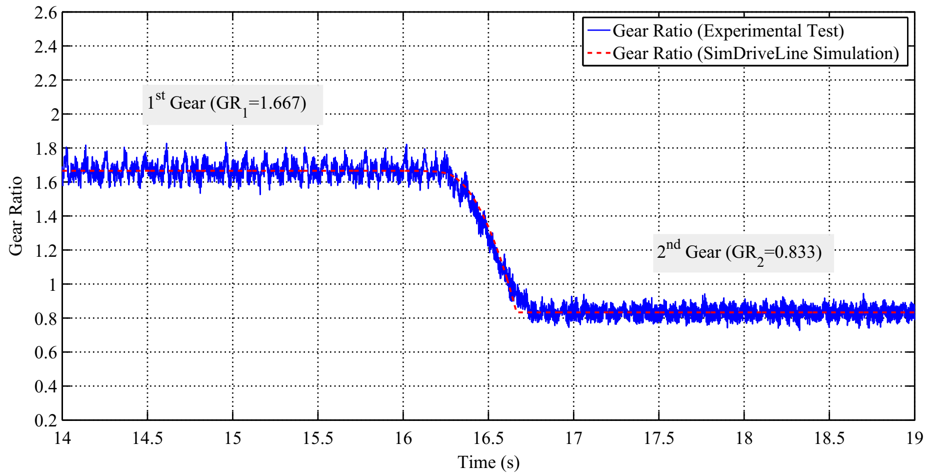

Fig. 11. The variation of the gear ratio (GR) for the upshift operation.

In Eqs. (57), (61) and (62) the first back stepping variable can be seen in the equations as follows:

$$\begin{cases} \dot{\omega}_w = -K_I\left(\omega_w - \omega_{w,des}\right) + \dfrac{i_{fd}}{J_v}\varpi \\ \dot{\varpi} = -i_{fd}K_o\omega_w + K_o\omega_{C,out} - \dot{\Phi} \end{cases}. \tag{63}$$

By incorporation of ϖ in the Lyapunov function:

$$V_2(\omega_w, \varpi) = \frac{1}{2}\left(\omega_w - \omega_{w,des}\right)^2 + \frac{1}{2}(\varpi)^2 \tag{64}$$

and considering a CLF for the second order sub systems Eq. (63):

$$\Upsilon = \omega_{C,out,des} = -\frac{i_{fd}}{K_o J_v}\left(\omega_w - \omega_{w,des}\right) + i_{fd}\omega_w + \frac{1}{K_o}\dot{\Phi} - \frac{K_{II}}{K_o}\varpi \tag{65}$$

the Lyapunov function time derivative becomes negative definite:

$$\dot{V}_2(\omega_w, \varpi) = -K_I\left(\omega_w - \omega_{w,des}\right)^2 - K_{II}\varpi^2 \tag{66}$$

and clearly ensures that $(\omega_w, \varpi) = (\omega_{w,des}, 0)$ is asymptotically stable.

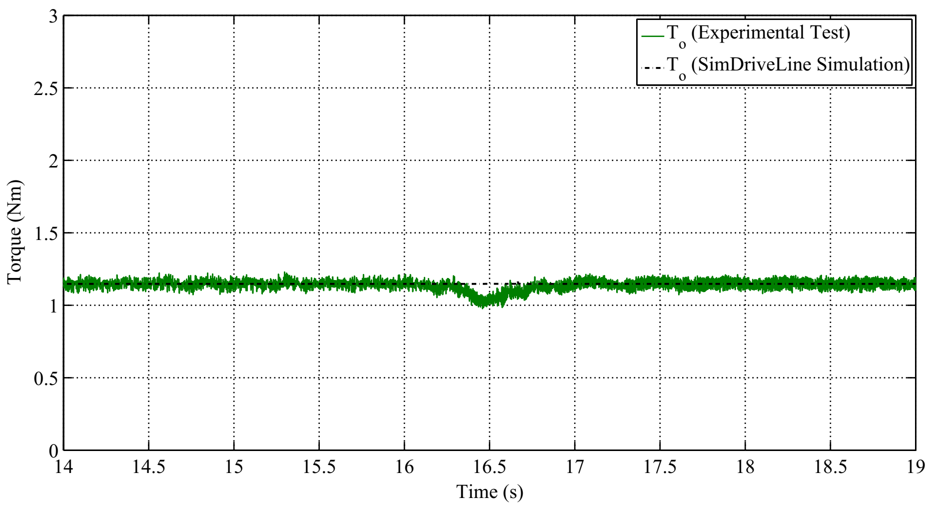

Fig. 12. The output torque (T_o) for the upshift operation.

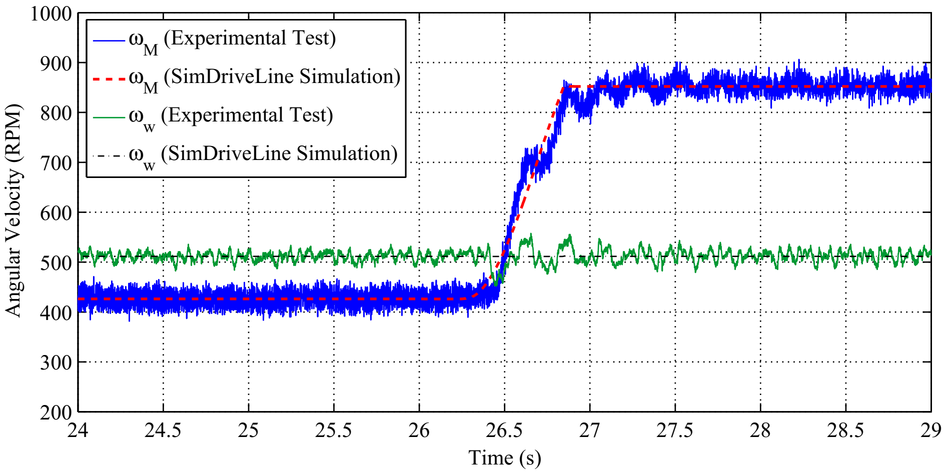

Fig. 13. The motor (ω_M) and output (ω_w) speeds for the downshift operation.

In order to proceed with the second backstep, the second change of variable is considered as:

$$\sigma = \omega_{C,out} - \omega_{C,out,des} = \omega_{C,out} - \Upsilon. \tag{67}$$

The Eqs. (23), (63) and (65) give:

$$\begin{cases} \dot{\omega}_w = -K_I\left(\omega_w - \omega_{w,des}\right) + \dfrac{i_{fd}}{J_v}\varpi \\ \dot{\varpi} = -K_{II}\varpi - \dfrac{i_{fd}}{J_v}\left(\omega_w - \omega_{w,des}\right) + K_o\sigma \\ \dot{\sigma} = A_\sigma + B_\sigma T_d + C_\sigma(\varpi + \Phi) - \dot{\Upsilon} \end{cases} \tag{68}$$

with:

$$\begin{cases} A_\sigma = \dfrac{1}{a(R_2+1)}((R_2\gamma - \lambda)T_{BR} + (\tau - R_2\lambda)T_{BS} \\ \qquad +(R_2\lambda - \tau)C_S\omega_S + (\lambda - R_2\gamma)C_R\omega_R \\ \qquad +(R_2\gamma - \lambda)T_{Rf} + (\tau - R_2\lambda)T_{Sf}) \\ B_\sigma = \dfrac{R_2 e + c}{a(R_2+1)} \\ C_\sigma = -\dfrac{R_2 f + d}{a(R_2+1)}. \end{cases} \tag{69}$$

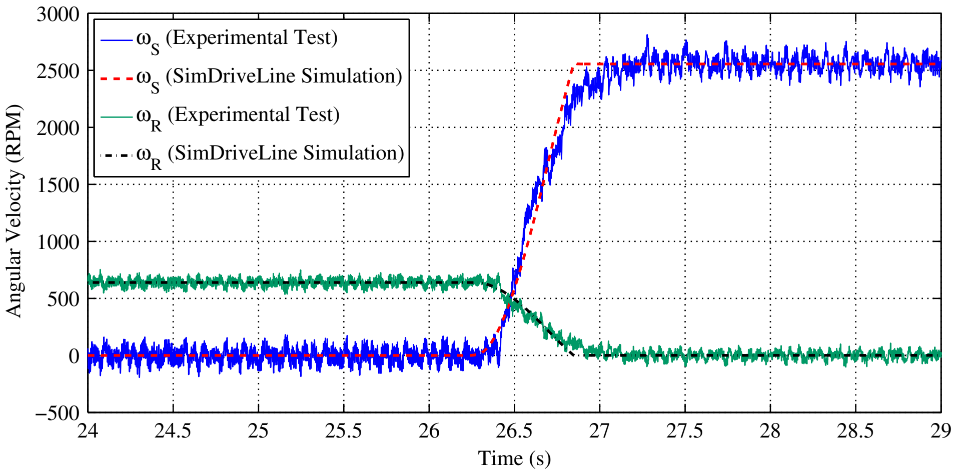

Fig. 14. The ring (ω_R) and sun (ω_S) speeds for the downshift operation.

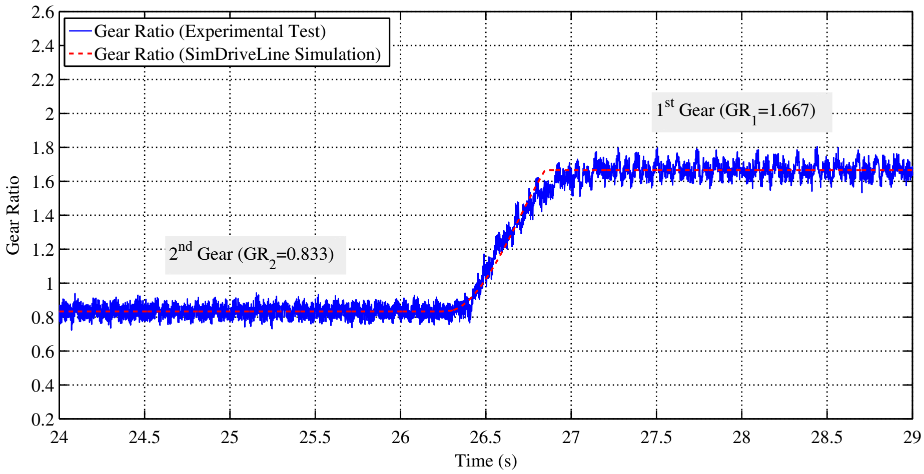

Fig. 15. The variation of the gear ratio (GR) for the downshift operation.

A candidate Lyapunov function to ensure the stability of the system Eq. (68) is:

$$V_3 = \frac{1}{2}\left(\omega_w - \omega_{w,des}\right)^2 + \frac{1}{2}(\varpi)^2 + \frac{1}{2}(\sigma)^2 \tag{70}$$

and applying the virtual control law:

$$\Psi = T_{d,des} = \frac{1}{B_\sigma}\left(-A_\sigma - K_o\varpi - C_\sigma(\varpi + \Phi) + \dot{\Upsilon} - K_{III}\sigma\right) \tag{71}$$

makes the Lyapunov derivative negative definite:

$$\dot{V}_3 = -K_I\left(\omega_w - \omega_{w,des}\right)^2 - K_{II}(\varpi)^2 - k_{III}(\sigma)^2 \tag{72}$$

which clearly ensures the asymptotically stability of the system Eq. (68) around the point $(\omega_w, \varpi, \sigma) = (\omega_{w,des}, 0, 0)$.

Considering the next backstepping change of variables as:

$$\zeta = T_d - T_{d,des} = T_d - \Psi \Rightarrow \dot{\zeta} = \dot{T}_d - \dot{\Psi} \tag{73}$$

transforms the system Eq. (68) to (according to Eq. (23)):

$$\begin{cases} \dot{\omega}_w = -K_I\left(\omega_w - \omega_{w,des}\right) + \dfrac{i_{fd}}{J_v}\varpi \\ \dot{\varpi} = -K_{II}\varpi - \dfrac{i_{fd}}{J_v}\left(\omega_w - \omega_{w,des}\right) + K_o\sigma \\ \dot{\sigma} = -K_{III}\sigma - K_o\varpi + B_\sigma\zeta \\ \dot{\zeta} = K_d\omega_M - K_d\omega_{C,in} - \dot{\Psi} \end{cases} . \tag{74}$$

Choosing the CLF as follows:

$$\Gamma = \omega_{M,des} = \frac{1}{K_d}\left(K_d\omega_{C,in} + \dot{\Psi} - B_\sigma\sigma - K_{IV}\zeta\right) \tag{75}$$

for the candidate Lyapunov function:

$$V_4 = \frac{1}{2}\left(\omega_w - \omega_{w,des}\right)^2 + \frac{1}{2}(\varpi)^2 + \frac{1}{2}(\sigma)^2 + \frac{1}{2}(\zeta)^2 \tag{76}$$

ensures the stability of the system Eq. (74) by making the derivative of the Lyapunov function Eq. (76) negative definite:

$$\dot{V}_4 = -K_I\left(\omega_w - \omega_{w,des}\right)^2 - K_{II}(\varpi)^2 - k_{III}(\sigma)^2 - K_{IV}\zeta^2. \tag{77}$$

The last backstepping change of variable is considered as:

$$\xi = \omega_M - \omega_{M,des} = \omega_M - \Gamma \Rightarrow \dot{\xi} = \dot{\omega}_M - \dot{\Gamma} \tag{78}$$

which transforms the system Eqs. (23) and (74) to

$$\begin{cases} \dot{\omega}_w = -K_I\left(\omega_w - \omega_{w,des}\right) + \dfrac{i_{fd}}{J_v}\varpi \\ \dot{\varpi} = -K_{II}\varpi - \dfrac{i_{fd}}{J_v}\left(\omega_w - \omega_{w,des}\right) + K_o\sigma \\ \dot{\sigma} = -K_{III}\sigma - K_o\varpi + B_\sigma\zeta \\ \dot{\zeta} = -K_{IV}\zeta - B_\sigma\sigma + K_d\xi \\ \dot{\xi} = \dfrac{1}{J_M}\left(T_M - (\Psi + \zeta)\right) - \dot{\Gamma} \end{cases}. \tag{79}$$

Considering the motor torque as:

$$T_M = (\Psi + \zeta) + J_M\left(-K_d\zeta + \dot{\Gamma} - K_V\xi\right) \tag{80}$$

makes the derivative of the candidate Lyapunov function:

$$V_5 = \frac{1}{2}\left(\omega_w - \omega_{w,des}\right)^2 + \frac{1}{2}(\varpi)^2 + \frac{1}{2}(\sigma)^2 + \frac{1}{2}(\zeta)^2 + \frac{1}{2}(\xi)^2 \tag{81}$$

negative definite as follows:

$$\dot{V}_5 = -K_I\left(\omega_w - \omega_{w,des}\right)^2 - K_{II}(\varpi)^2 - k_{III}(\sigma)^2 - K_{IV}\zeta^2 - K_V\xi^2 \tag{82}$$

which clearly ensures asymptotic stability of the dynamical system Eq. (79):

$$(\omega_w, \varpi, \sigma, \zeta, \xi) \rightarrow \left(\omega_{w,des}, 0, , , 0, , , 0, , , 0\right).$$

The motor torque in Eq. (80) is equivalent to:

$$T_M = T_d + J_M\left(-K_d\left(T_d - T_{d,des}\right) + \dot{\omega}_{M,des} - K_V\left(\omega_M - \omega_{M,des}\right)\right). \tag{83}$$

5. Simulation and experimental results

In the simulation analysis, the driveline of an electric vehicle equipped with the transmission proposed in this paper, as shown in Fig. 1, has been modeled in MATLAB/*Simulink®* by utilizing the SimDriveLine library. The MATLAB/*Simulink®* model is depicted in Fig. 5.

The experimental apparatus shown in Fig. 6 is developed at the Centre for Intelligent Machines (CIM) of McGill University and it is composed of two planetary gear sets with common ring and common sun gears. The ratios of the first and the second planetary gears, as mentioned in Section 2, are $R_1 = 2$ and $R_2 = 4$, respectively. Two motors are connected to the input and output carriers of the transmission where the motor connected to the input carrier replaces the main traction motor in the vehicle, and the motor connected to the output carrier is used to mimic the loads on the vehicle. The traction and load motors are identical with the rated torque 2.1 Nm, the rated speed 314 rad/s and the moment of inertia 5.9×10^{-5} kg·m^2. The brake actuators are linear solenoids for which the relation between the applied current to the solenoid and the resulting force in 5 mm air gap is measured experimentally and the fitted curve to the experimental data has the following relation:

$$F = -8.097I^3 + 47.73I^2 - 21.13I \tag{84}$$

where F is the magnetic force of the solenoid in Newtons and I is the applied current in Amperes. The brake of the sun is designed to be of the multi-plate brake type with 4 friction surfaces illustrated in Fig. 7(a). The brake of the ring gear is designed to be of the band brake type with the wrap angle 4.014 (rad) which is shown in Fig. 7(b).

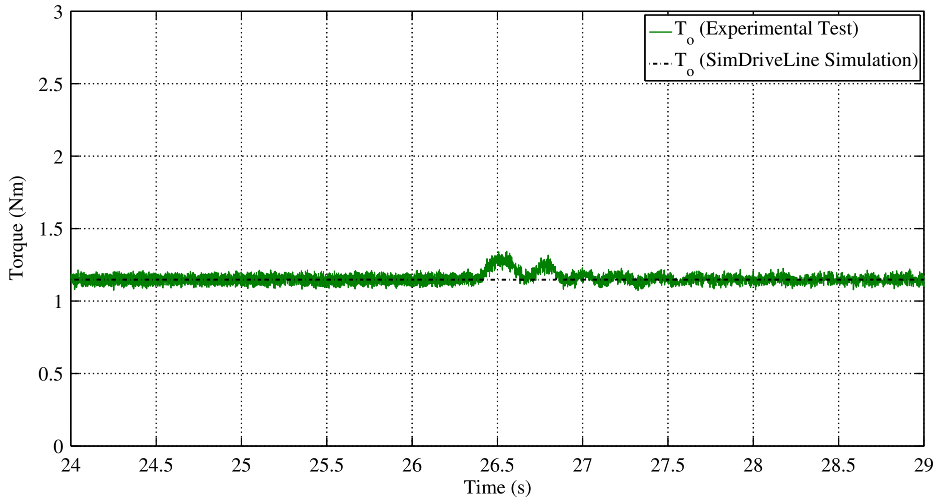

Fig. 16. The output torque (T_o) for the downshift operation.

For the apparatus shown in Fig. 6, the values of the mass and moment of inertia of the components, the Coulomb and viscous friction models and the coefficient of the friction of the brakes are estimated based on the time domain input–output data in MATLAB System Identification Toolbox. The stiffness and damping parameters of the input and output shafts are acquired from the datasheets and the radii of the drum of the band brake, the brake plates and the gears are obtained by direct measurements. The mass and moment of inertia of the components are verified with their 3D CAD models. The obtained parameters are listed in Table 2.

The simulation and experimental tests are carried out for a sample drive cycle with a duration of 50 s which has one upshift at $t =$ 16 s and one downshift at $t = 26$ s. The resisting torque of the load motor is considered to be a quadratic function of the angular velocity with the equation $T_v = 0.0004\omega_w^2 Nm$ in order to mimic the aerodynamic drag torque on the vehicle which is the dominant resisting load at high speeds [12,37].

The designed backstepping controller with the parameters given in Table 3 is applied to both experimental and simulation tests to maintain the output torque and the output speed constant. The applied brake forces for both experimental and simulation tests are shown in Fig. 8 with $N_{BS,\max} = 110$ N and $N_{BR,\max} = 30$ N.

For practical reasons, instead of direct measurement of the torques on the input and the output shafts, an stochastic observer is employed in order to estimate T_d and T_o from the dynamical Eq. (23) using the measured values of the states ω_M and ω_w and the known values of the input torques T_M, T_{BS} and T_{BR}.

For clarity of the figures, the results of the mathematical model are not shown because they exactly fit the simulation results from the SimDriveLine model.

The simulation and experimental results for the upshift process are illustrated in Figs. 9–12 and the results of the downshift operation are demonstrated in Figs. 13–16. The frequency of data acquisition for both experimental and simulation tests are 1000 Hz. The motor (ω_M) and output (ω_w) speeds during the upshift and downshift operations are illustrated in Figs. 9 and 13. It can be observed

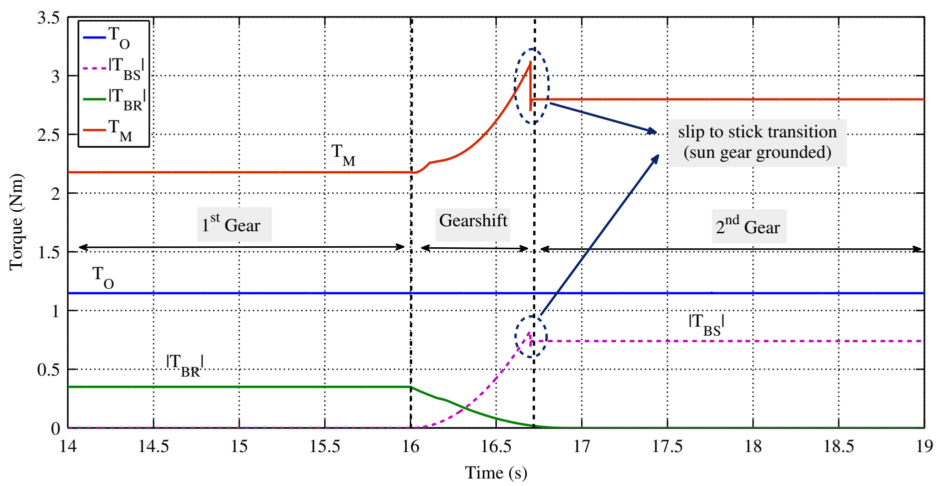

Fig. 17. Simulated brake friction torque and motor torque for the upshift operation.

that during the synchronization of the motor with the speed of the driveline in the target gear, the designed controller effectively maintained the output speed to such a point that the oscillation of the output speed at 511 RPM is suppressed in the simulation analysis, and in the experimental test, it remains less than 10%. It should be noted that, unlike the torque and inertia phases in controlling DCTs and ATs, in the proposed transmission, synchronization of the motor speed and switching the brakes happen simultaneously as discussed in Section 4.

In Fig. 8, disengagement of the off-going brake and engagement of the oncoming brakes start at $t = 16$ s and $t = 26$ s for the upshift and downshift operations, respectively. However, the synchronization of the motor starts later than $t = 16$ s and $t = 26$ s in Figs. 9 and 13. This delay corresponds to the time reserved for the preparation of the oncoming and off-going brakes. In other words, this delay is related to pre-fill the oncoming brake and to bring the off-going brake to slip mode. By considering the time of preparation of the oncoming and off-going brakes in the shifting time, the upshift and downshift processes last respectively about 0.6 s and 0.8 s in the simulation, and they take about 0.8 s and 1 s in the experimental test.

The angular velocities of the ring (ω_R) and sun (ω_S) gears for the upshift and downshift operations are shown in Figs. 10 and 14. It can be seen that during the upshift process the sun gear is grounded and the ring gear is released and the opposite case holds for the downshift operation.

The variation of the gear ratio for the upshift and downshift processes are demonstrated in Figs. 11 and 15, respectively. This variation can be used as a criterion to measure the duration of the gear changing process.

The output torque for the upshift and downshift operations are illustrated in Figs. 12 and 16. It can be seen that the oscillation of the output torque during the gear changing process in the simulation is negligible and in the experimental test, it remains less than 15%. The oscillation of the output torque and output speed and the increase in the shifting time in the experimental test in comparison to simulation results come from unmodeled uncertainties in the dynamical model of the system and actuators, such as unmodeled uncertainties in the complex friction model of the internal gears, the variation of the viscosity of the transmission oil used for the experimental test by increasing the temperature, uncertainties in the position of the solenoid's plunger due to compression of the multi brake plates and deformation of the band which results in the deviation of T_{BS} and T_{BR} from the desired values, and unmodeled uncertainties in the resistance of the solenoid actuators which comes from the variation of the temperature of the coil which causes uncertainness in the resulting force.

Transitions between slip and stick phases at the end of gear shifting operation in the experimental results are different from the theoretical results (i.e., the simulation results) in the upshift process in Figs. 9–11 and the downshift in Figs. 13–15. These differences are due to the consideration of friction torques in simulations in the form of Coulomb and Stribeck friction [38,39], that is not an exact representative of the behavior of frictional torques of the brakes in the experimental testbed.

Brake friction torque, the motor torque applied to both the computer model and the experimental setup, and the simulated output torque of the transmission are illustrated in Figs. 17 and 18 for the upshift and downshift operations, respectively. As illustrated in these figures, the additional motor torque required for the compensation of the slip friction on the brakes disappears at the end of gear shifting process when the oncoming brake comes to rest in the stick mode.

The effect of engagement and disengagement intervals of the oncoming and off-going brakes from 0.1 s to 1.5 s (0.1, 0.3, 0.6, 0.9, 1.2, and 1.5) on the shifting time and the energy dissipation for the upshift and downshift processes are illustrated in Fig. 19. It can be seen that increasing the engagement and disengagement intervals from 0.1 s to 1.5 s increases the shifting time from 0.18 s to 1.04 s for the upshift process and 0.46 s to 1.53 s for the downshift operation. The growth of the energy dissipation caused by the internal brakes of the transmission during the gear changing process are from 51.7 J to 96.23 J and from 18.8 J to 36.83 J for the upshift and downshift operations, respectively. This verifies that the smallest interval i.e., the case with sudden engagement and disengagement of the oncoming and off-going brakes corresponds to the minimum shifting time and minimum dissipated energy, as indicated by the results of the Pontryagin Minimum Principle in Section 4.

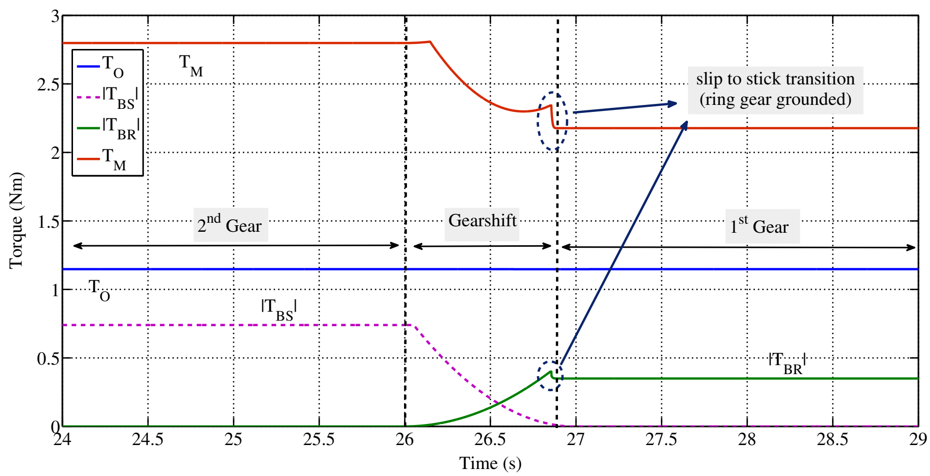

Fig. 18. Simulated brake friction torque and motor torque for the downshift operation.

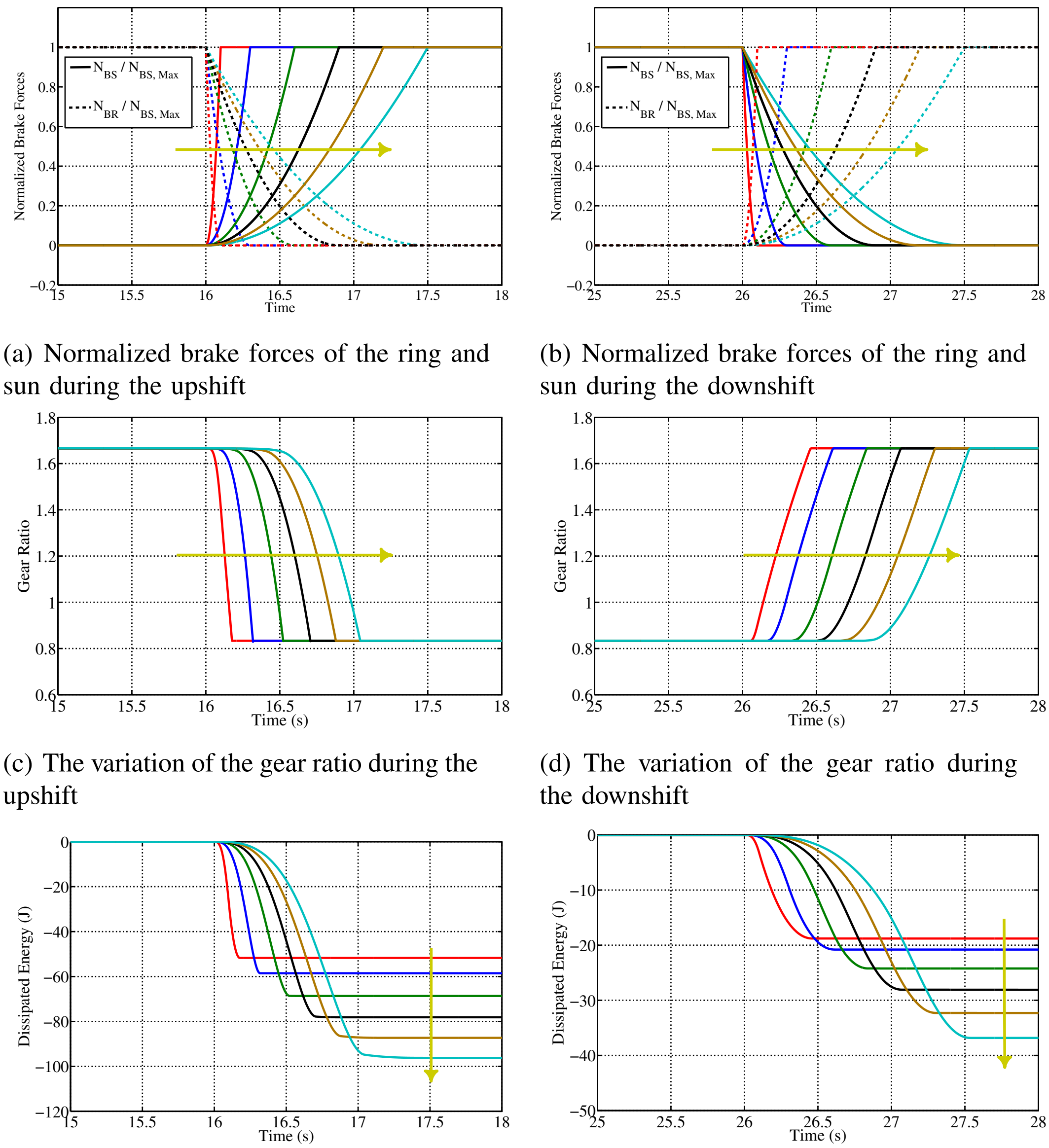

(a) Normalized brake forces of the ring and sun during the upshift

(b) Normalized brake forces of the ring and sun during the downshift

(c) The variation of the gear ratio during the upshift

(d) The variation of the gear ratio during the downshift

(e) The dissipated energy during the upshift

(f) The dissipated energy during the downshift

Fig. 19. The effect of engagement and disengagement intervals of the oncoming and off-going brakes on the shifting time and energy dissipation.

6. Conclusion

In this paper, a novel seamless two-speed transmission for electric vehicles is proposed. Kinematic analysis of the transmission and achievable gear ratios are presented. The analytical dynamic model of the driveline of an electric vehicle equipped with the proposed transmission is derived based on kinematic analysis and by utilizing the torque balance and virtual work principle. Thereafter, the Pontryagin Minimum Principle is used to derive an optimal control law to minimize the shifting time and the energy dissipation during the gear changing process while keeping the output speed and output torque constant. The optimal control problem results in a bang–bang type control law for the oncoming and off-going brakes while the corresponding optimal trajectories for T_d and T_o maintain the output speed and output torque constant during the gear change. In order to provide a closed-loop controller based on the results of the Pontryagin Minimum Principle and due to the recursive and nonlinear dynamics of the driveline in Eq. (23) the backstepping method is applied to design a controller that tracks the optimal trajectories while relaxing the abrupt changes in the control inputs to cope with the actuator limitations.

The mathematical model of the driveline has been validated with experimental tests and SimDriveLine library of MATLAB/*Simulink*® and the performance of the designed controller has been evaluated. The simulation results indicate that the torque hole is almost eliminated in both experimental and simulation results while the oscillation of the output torque and output speed during the gear changing is negligible. While a completely seamless operation is shown to exist theoretically, due to uncertainties in the modeling of the system and actuators in the experimental test rig the output speed and output torque deviate from their desired values in amounts less than 10% and 15%, respectively.

In the study the effect of engagement and disengagement intervals of the oncoming and off-going brakes, simulation results indicate that increasing the engagement and disengagement intervals of the oncoming and off-going brakes will increase the shifting time and the energy dissipation caused by the internal brakes of the transmission dramatically. The minimum shifting time and the energy dissipation corresponds to the sudden engagement and disengagement of the brakes as expected from the results of the Pontryagin Minimum Principle.

Further research on this topic is under development at the Centre for Intelligent Machines (CIM) of McGill University in the following three phases:

Phase I Designing an H_∞ robust controller to reject disturbances and noise and cover uncertainties in the modeling of the systems and actuators.
Phase II Estimation of the braking torques in order to improve the shifting quality.
Phase III Analysing the performance of the proposed transmission with the designed controllers in the actual vehicle scale equipped with torque transducer.

Acknowledgment

The authors would like to thank the support of the industrial partners: Linamar, TM4 and Infolytica. The authors would also like to thank Mr. Tyler Clancy for his assistance in improving the braking mechanism of the transmission. The research work reported here is supported the Natural Sciences and Engineering Research Council of Canada (NSERC) and the Automotive Partnership Canada (APC) (APCPJ 418901-11).

References

[1] P.D. Walker, S. Abdul Rahman, B. Zhu, N. Zhang, Modelling, simulations, and optimisation of electric vehicles for analysis of transmission ratio selection, Adv. Mech. Eng. 5 (2013) 1–13.
[2] X. Zhou, P. Walker, N. Zhang, B. Zhu, J. Ruan, Numerical and experimental investigation of drag torque in a two-speed dual clutch transmission, Mech. Mach. Theory 79 (2014) 46–63.
[3] B. Gao, Q. Liang, Y. Xiang, L. Guo, H. Chen, Gear ratio optimization and shift control of 2-speed I-AMT in electric vehicle, Mech. Syst. Signal Process. 50 (2015) 615–631.
[4] M.S. Rahimi Mousavi, B. Boulet, Modeling, simulation and control of a seamless two-speed automated transmission for electric vehicles, American Control Conference (ACC), 2014, IEEE 2014, pp. 3826–3831.
[5] M.S. Rahimi Mousavi, A. Pakniyat, B. Boulet, Dynamic modeling and controller design for a seamless two-speed transmission for electric vehicles, Control Applications (CCA), 2014 IEEE Conference on, IEEE 2014, pp. 635–640.
[6] H. Naunheimer, B. Bertsche, J. Ryborz, W. Novak, Automotive Transmissions: Fundamentals, Selection, Design and Application, Springer Science & Business Media, 2010.
[7] G. Lucente, M. Montanari, C. Rossi, Modelling of an automated manual transmission system, Mechatronics 17 (2) (2007) 73–91.
[8] J. Zhang, L. Chen, G. Xi, System dynamic modelling and adaptive optimal control for automatic clutch engagement of vehicles, Proc. Inst. Mech. Eng. J. Automob. Eng. 216 (12) (2002) 983–991.
[9] A. Ge, H. Jin, Y. Lei, Engine constant speed control in starting and shifting process of automated mechanical transmission (AMT), FISITA World Automotive Congress, Seoul, 2000.
[10] C.-H. Yu, C.-Y. Tseng, C.-P. Wang, Smooth gear-change control for EV clutchless automatic manual transmission, Advanced Intelligent Mechatronics (AIM), 2012 IEEE/ASME International Conference on, IEEE 2012, pp. 971–976.
[11] X. Zhu, H. Zhang, J. Xi, J. Wang, Z. Fang, Optimal speed synchronization control for clutchless AMT systems in electric vehicles with preview actions, American Control Conference (ACC), 2014, IEEE 2014, pp. 4611–4616.
[12] M. Kulkarni, T. Shim, Y. Zhang, Shift dynamics and control of dual-clutch transmissions, Mech. Mach. Theory 42 (2) (2007) 168–182.
[13] E. Galvagno, M. Velardocchia, A. Vigliani, Dynamic and kinematic model of a dual clutch transmission, Mech. Mach. Theory 46 (6) (2011) 794–805.
[14] P.D. Walker, N. Zhang, R. Tamba, Control of gear shifts in dual clutch transmission powertrains, Mech. Syst. Signal Process. 25 (6) (2011) 1923–1936.
[15] B. Zhu, N. Zhang, P. Walker, W. Zhan, X. Zhou, J. Ruan, Two-speed dct electric powertrain shifting control and rig testing, Adv. Mech. Eng. 5 (2013) 1–10.
[16] N. Srivastava, I. Haque, A review on belt and chain continuously variable transmissions (cvt): dynamics and control, Mech. Mach. Theory 44 (1) (2009) 19–41.
[17] G. Carbone, L. Mangialardi, B. Bonsen, C. Tursi, P. Veenhuizen, Cvt dynamics: theory and experiments, Mech. Mach. Theory 42 (4) (2007) 409–428.
[18] N. Srivastava, I. Haque, Transient dynamics of metal v-belt cvt: effects of band pack slip and friction characteristic, Mech. Mach. Theory 43 (4) (2008) 459–479.
[19] T. Chen, D. Lee, C. Sung, An experimental study on transmission efficiency of a rubber v-belt cvt, Mech. Mach. Theory 33 (4) (1998) 351–363.
[20] G. Jung, B. Cho, K. Lee, Dynamic analysis and closed-loop shifting control of ef-automatic transmission with proportional control solenoid valves, FISITA World Automotive Congress, Seoul, Korea 2000, pp. 12–15.
[21] A. Haj-Fraj, F. Pfeiffer, Dynamic modeling and analysis of automatic transmissions, Advanced Intelligent Mechatronics, 1999. Proceedings. 1999 IEEE/ASME International Conference on, IEEE 1999, pp. 1026–1031.
[22] C. Lazar, C.-F. Caruntu, A.-E. Balau, Modelling and predictive control of an electro-hydraulic actuated wet clutch for automatic transmission, Industrial Electronics (ISIE), 2010 IEEE International Symposium on, IEEE 2010, pp. 256–261.
[23] H.A. Asl, N.L. Azad, J. McPhee, Modeling torque converter characteristics in automatic drivelines: lock-up clutch and engine braking simulation, ASME 2012 International Design Engineering Technical Conferences and Computers and Information in Engineering ConferenceAmerican Society of Mechanical Engineers 2012 359–367.
[24] N. Zhang, A. Crowther, D. Liu, J. Jeyakumaran, A finite element method for the dynamic analysis of automatic transmission gear shifting with a four-degree-of-freedom planetary gearset element, Proc. Inst. Mech. Eng. D J. Automob. Eng. 217 (6) (2003) 461–473.
[25] M.-C. Tsai, C.-C. Huang, B.-J. Lin, Kinematic analysis of planetary gear systems using block diagrams, J. Mech. Des. 132 (6) (2010) 065001.

[26] A. Pakniyat, P.E. Caines, The gear selection problem for electric vehicles: an optimal control formulation, Control Automation Robotics & Vision (ICARCV), 2014 13th International Conference on, IEEE 2014, pp. 1261–1266.
[27] J. Oh, J. Kim, S. Choi, Design of estimators for the output shaft torque of automated manual transmission systems, Industrial Electronics and Applications (ICIEA), 2013 8th IEEE Conference on, IEEE 2013, pp. 1370–1375.
[28] C. Lanczos, The Variational Principles of Mechanics, vol. 4, Courier Corporation, 1970.
[29] R. Bundynas, K. Nisbett, Shigleys Mechanical Engineering Design, 2009.
[30] H. Jibin, P. Zengxiong, W. Chao, Experimental research on drag torque for single-plate wet clutch, J. Tribol. 134 (1) (2012) 014502.
[31] Paul D. Walker, Nong Zhang, Ric Tamba, Simon Fitzgerald, Simulations of drag torque affecting synchronisers in a dual clutch transmission, Jpn. J. Ind. Appl. Math. 28 (1) (2011) 119–140.
[32] S. Iqbal, F. Al-Bender, B. Pluymers, W. Desmet, Model for predicting drag torque in open multi-disks wet clutches, J. Fluids Eng. 136 (2) (2014) 021103.
[33] R. Andrzejewski, J. Awrejcewicz, Nonlinear Dynamics of a Wheeled Vehicle, vol. 10, Springer Science & Business Media, 2006.
[34] J.J. Oh, S.B. Choi, J. Kim, Driveline modeling and estimation of individual clutch torque during gear shifts for dual clutch transmission, Mechatronics 24 (5) (2014) 449–463.
[35] D. Kirk, Optimal Control Theory. An Introduction, 1970.
[36] M. Shahid Shaikh, P.E. Caines, On the hybrid optimal control problem: theory and algorithms, IEEE Trans. Autom. Control 52 (9) (2007) 1587–1603.
[37] G. Kadijk, N. Ligterink, Road load determination of passenger cars, TNO Report: TNO 2012, p. R10237.
[38] H. Olsson, K.J. Åström, C.C. De Wit, M. Gäfvert, P. Lischinsky, Friction models and friction compensation, Eur. J. Control. 4 (3) (1998) 176–195.
[39] E. Berger, Friction modeling for dynamic system simulation, Appl. Mech. Rev. 55 (6) (2002) 535–577.